Chalcohalide Antiperovskite Thin Films with Visible Light Absorption and High Charge-Carrier Mobility Processed by Solvent-Free and Low-Temperature Methods

Paz Sebastiá-Luna,[a] Nathan Rodkey,[a,b] Adeem Saeed Mirza,[b] Sigurd Mertens,[c] Snigdha Lal,[d] Axel Melchor Gaona Carranza,[a] Joaquín Calbo,[a] Marcello Righetto,[d] Michele Sessolo,[a] Laura M. Herz,[d,e] Koen Vandewal,[c] Enrique Ortí,[a] Mónica Morales-Masis,[b] Henk J. Bolink,[a]* and Francisco Palazon[a,f]*

[a] Instituto de Ciencia Molecular, Universidad de Valencia, 46980 Paterna, Spain

[b] MESA+ Institute for Nanotechnology, University of Twente, Enschede 7500 AE, The Netherlands

[c] Institute for Materials Research (IMO-IMOMEC), Hasselt University, Diepenbeek BE – 3590, Belgium

[d] Department of Physics, University of Oxford, Clarendon Laboratory, Parks Road, Oxford OX1 3PU, UK.

[e] Institute for Advanced Study, Technical University of Munich, Lichtenbergstrasse 2a, D-85748 Garching, Germany.

[f] Departamento de Ingeniería Química y Ambiental, Universidad Politécnica de Cartagena, 30202 Cartagena, Spain

ABSTRACT: Silver chalcohalide antiperovskites represent a rather unexplored alternative to lead halide perovskites and other semiconductors based on toxic heavy metals. All synthetic approaches reported so far for Ag_3SI and Ag_3SBr require long synthesis times (typically days, weeks or even months) and high temperatures. Herein, we report the synthesis of these materials using a fast and low-temperature method involving mechanochemistry. Structural and optical properties are examined experimentally and supported by first principles calculations. Furthermore, we deposit Ag_3SI as thin films by pulsed laser deposition and characterize its optoelectronic properties using optical-pump-terahertz-probe measurements, revealing a high charge-carrier mobility of 49 $cm^2V^{-1}s^{-1}$. This work paves the way to the implementation of chalcohalide antiperovskites in various optoelectronic applications.

1. INTRODUCTION

Lead halide perovskites have marked a revolution in optoelectronics and other energy-related applications in the last decade. Much of the success of these materials can be related to the extraordinary versatility of the perovskite structure which allows for a broad range of related crystal phases (*e.g.,* tetragonal and orthorhombic distortions) and chemical compositions (*e.g.,* multi-cation and/or multi-anion compositions). Yet, beyond lead halide perovskites, there exists a number of analogous compounds, many of which remain relatively underexplored.[1] This is the case of the antiperovskite structure, where "anti" refers to the swapped positions of the anions and cations in the ABX_3 structure (see Figure 1).

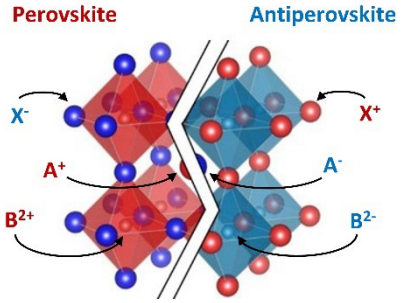

Figure 1. Schematic representation of halide perovskite (left) and chalcohalide antiperovskite (right) crystal structures. The antiperovskite structure can be viewed as a perovskite structure where anions (in red) are replaced by cations (in blue) and viceversa.

As is also true for lead halide perovskites,[2] chalcohalide antiperovskites are not newly discovered materials. Indeed, Ag_3SI and Ag_3SBr, which adopt the antiperovskite structure, have been reported at least since 1960 (note that these can also be written as $ISAg_3$ and $BrSAg_3$ to stress the analogy with the more typical ABX_3 representation of the perovskite structure).[3] Nevertheless, the vast majority of synthesis methods reported so far are carried out in a quartz tube sealed under vacuum and require very high temperatures,

often substantially above 200 °C and long synthesis times (see Table 1), which make these processes unsuitable for most applications.

Table 1. Summary of reported synthesis conditions for Ag_3SI and Ag_3SBr. The maximum temperatures achieved during each synthesis and their total time are given.

Material	Maximum temperature (°C)	Total time	References
Ag_3SI, Ag_3SBr	200	1 month	[4,5]
Ag_3SBr	220	10 days	[6]
Ag_3SI, Ag_3SBr	280	2 months	[7,8]
Ag_3SI, Ag_3SBr	300	4–5 days	[9–11]
Ag_3SBr	300	10 days	[12]
Ag_3SI, Ag_3SBr	400	4–5 days	[13,14]
Ag_3SI	550	17 hours	[15]
Ag_3SI, Ag_3SBr	550	5–7 days	[16–18]
Ag_3SI	600	1 day	[18]
Ag_3SI	700	3 months	[19]
Ag_3SI	750	3 hours	[20]
Ag_3SI	800	6–7 days	[21,22]
Ag_3SBr	800	6 months	[23,24]
Ag_3SBr	800	1 month	[25]
Ag_3SBr	800	4 months	[26]
Ag_3SI	850	30 hours	[27]
Ag_3SI, Ag_3SBr	Digestion - 200	2–3 days	[7,27–31]

The main interest in these materials so far has been related to their relatively high ionic conductivity first reported by Takahashi and Yamamoto in 1966.[15] Most of the later work has been focused on elucidating the crystallography and phase transitions of these antiperovskites. Regarding Ag_3SI, at least 4 polymorphs have been reported commonly denoted as α-, α*-, β-, and γ-phases which structurally differ in the ordering of the different ions.[32] The α phase, with disordered S^{2-}/I^- anions, is reported to be the most stable at temperatures above 250 °C. Upon cooling to room temperature, α-Ag_3SI may convert to the reportedly more stable β-phase with ordered anions and lower ionic conductivity, or transform into the metastable α* phase, which has disordered S^{2-}/I^- anions (and higher ionic conductivity) similar to the high-temperature α phase but differs in the position of the Ag^+ cations. The γ phase, which features Ag^+ cation ordering, is only reported at low temperatures (< 128 K).[33] Electrical conductivity in all cases has been mainly attributed to ionic movement. Regarding optical properties, Ag_3SI is reported to be a narrow-bandgap semiconductor with theoretically- and experimentally-determined direct bandgaps around 0.9–1.1 eV at room temperature,[14,34] making it especially promising for photovoltaics. Ag_3SBr appears to be less studied in comparison with scarce and conflicting bandgap energies reported from 0.3 eV to 1.9 eV.[35–37] Eventually, regarding the deposition of thin films, we are only aware of one report by Tver'yanovich *et al.*[20] on multilayer films lacking detailed structural and/or elemental analysis.

In summary, silver chalcohalide antiperovskites appear promising as low-toxicity alternatives to lead halide perovskites for photovoltaics and other optoelectronic applications. Nevertheless, with regards to literature, it is obvious that for the potential implementation of these materials in such fields, it is paramount to synthesize antiperovskites in a much more time- and energy-efficient manner than those described in Table 1. Furthermore, the deposition of relevant thin films remains virtually unexplored. Finally, optoelectronic properties beyond ionic conductivity especially of thin film samples, are yet to be accurately determined.

Here, we demonstrate that Ag_3SBr and Ag_3SI antiperovskites can be synthesized as non-templated high-purity powders by fast and low-temperature processes combining mechanochemical synthesis and mild thermal annealing. Light-absorption properties of the obtained crystallites are characterized experimentally by photothermal deflection spectroscopy (PDS). Furthermore, Ag_3SI is deposited as thin films by pulsed laser deposition (PLD). Structural, morphological and elemental characterization are carried out using X-ray Diffraction (XRD), scanning electron microscopy (SEM), and energy-dispersive X-ray spectroscopy (EDS) demonstrating the formation of compact antiperovskite thin films with thicknesses in the hundreds of nanometers. Air photoelectron spectroscopy (APS), Kelvin probe measurements (KP), PDS as well as UV-vis spectroscopy are employed to gain some insights into the optical absorption properties and energy levels of Ag_3SI semiconductor thin films. Optical-pump-terahertz-probe (OPTP) measurements demonstrate for the first time the high charge-carrier mobility in these materials (note that reports on high mobilities so far have focused on ion mobilities which the terahertz probe is largely insensitive to) and reveal that charge carriers are short lived. Eventually, density functional theory (DFT) calculations are undertaken to shed more light into the optoelectronic properties of Ag_3SI and Ag_3SBr antiperovskites as well as on their dependence on structural disorder.

2. EXPERIMENTAL SECTION

Materials. Silver iodide (AgI 99.999%), silver sulfide (Ag2S, 99.9%), sulphur (99.99%), chlorobenzene (99.8%, anhydrous), and acetonitrile (anhydrous) were purchased from Sigma-Aldrich. Silver bromide (AgBr, > 99.998%) was pur-

chased from Alfa Aesar. All chemicals were stored in a nitrogen-filled glovebox and used as received without further purification.

Mechanochemical synthesis of Ag_3SBr and Ag_3SI. Stoichiometric amounts of Ag_2S and AgX (X = Br, I) was introduced inside 10 mL zirconia ball-mill jars with 2 zirconia beads of 10 mm in diameter. Powders were maintained in inert atmosphere, since the jars were closed inside a nitrogen-filled glovebox. Ball-milling (BM) was performed with a MM-400 shaking ball-mill from Retsch, at a frequency of 30 Hz for 1 h. Pure antiperovskite was formed after annealing under inert atmosphere for 30 min at 160 °C for Ag_3SI and 220 °C for Ag_3SBr.

XRD characterization. X-ray diffraction was measured with a powder diffractometer Empyrean from Panalytical equipped with CuKα anode operated at 45 kV and 40 mA. Single scans were acquired in the 2θ = 8 to 60° range with a step size of 2θ = 0.01° in Bragg-Brentano geometry in air. XRD analysis was carried out with Fullprof software.

Photothermal deflection spectroscopy (PDS). The PDS measurements were performed using a home-built setup. Monochromatic light originating from a 100 W Quartz-Tungsten-Halogen lamp in combination with an Oriel monochromator was chopped (8.2 Hz) and focused onto the sample. Samples consist of either thin films deposited on quartz substrates, or powders glued onto quartz substrates. A small amount of powder was used in order to create a surface as flat as possible. The samples are placed in a quart cuvette and submersed in perfluorohexane (C6F14, 3M Fluorinert FC-72). A HeNe (633 nm) probe laser grazes the surface of the sample. The monochromatic light is absorbed by the sample and produces a slight heating of the perfluorohexane, which has a strongly temperature dependent refractive index, resulting in a deflection of the probe laser proportional to the absorbed intensity. The amplitude of this deflection is detected by a position sensitive Si detector, which is connected to a Stanford Research Systems SR830 lock-in amplifier. The intensity of the monochromatic light is simultaneously measured by a pyro-electric detector. The normalized PDS-signal is obtained by the division of the deflection signal by the signal measured by the pyro-electric detector and is for weakly emissive samples proportional to the absorption spectrum.

Scanning Electron Microscopy (SEM) / Energy Dispersive X-ray Spectroscopy (EDX). High resolution SEM images were taken with Zeiss Merlin HR-SEM using the InLens detector mode and electron high tension (EHT) of 1.4kV. The atomic ratios were determined using EDX detector mode.

Theoretical calculations. Theoretical calculations were performed under the density functional theory (DFT) framework by means of the FHI-AIMS program suite. Initial crystal structures were extracted from Materials Project (IDs: mp-1105645 for Cmcm Ag3Br, mp-558189 for $Pm\bar{3}m$ Ag3SI, and mp-22995 for R3 Ag3SI). Primitive, conventional, and 2×2×2 conventional extended cells were modelled. Minimum-energy crystal geometries were obtained at the PBEsol/tier-1 level of theory upon full ionic and lattice vector length relaxation keeping the lattice vectors angles fixed.4 Single-point electronic structure calculations were performed on the optimized crystals at the PBEsol and HSE06 levels both without and with the spin-orbit coupling correction. In all the calculations, relativistic effects were considered by using the atomic ZORA approximation.2 To sample the first Brillouin zone, a 6×6×6 k-grid was employed for primitive and conventional unit cells, whereas a 1×1×1 k-grid was used in the extended cells, in both crystal optimizations and single-point calculations. Ab-initio Car-Parrinello molecular dynamics were performed for Ag_3SX conventional ORC unit cells under the Quantum Espresso 7.1 suite of packages. Prior to production, first an electronic relaxation (keeping fixed the atomic positions) was performed, and then a thermalization (NVE) simulation was carried out. The production dynamics was simulated along 1 ps in an NVT ensemble using the Nose-Hoover thermostat (T = 300 K). Plane-wave basis set and ultrasoft pseudo potentials based on the PBE parametrization were employed. Wavefunction and density cutoffs of 25 and 200 Ry were applied. 40 snapshots along the dynamics were extracted and the bandgap was computed in single-point calculations at the HSE06+SOC level in FHI-AIMS.

Thin-film deposition by pulsed laser deposition (PLD). To prepare the targets for PLD, fully-formed anti-perovskite powders with added elemental sulphur were pressed at ~600 MPa for 30 minutes. These targets are then ablated using a Coherent KrF excimer laser (λ = 248 nm) under vacuum in an Ar atmosphere. The working pressure was fixed to 1.5×10^{-2} mbar, the frequency to 10 Hz, and the spot-size to 1 mm2. The working pressure in particular was fixed at $1.5x10^{-2}$ mbar to remain in a pressure regime where dense film formation is expected.

Optical pump terahertz probe (OPTP) spectroscopy. An amplified 800 nm laser (Spectra physics – Mai Tai - Ascend - Spitfire) is used to generate 35 fs pulses at a repetition rate of 5 kHz. A spintronic emitter (2 nm tungsten, 18 nm Co40Fe40B20, 2 nm platinum on quartz) is used to convert the part of the 800 nm laser output into THz pulses. The THz setup is used in transmission configuration. The transmitted THz pulse is detected using electro-optic sampling. Here, another split-off of the 800 nm laser output (known as the gate beam) is overlapped with the transmitted THz pulse in a non-linear ZnTe crystal. The change in polarization of the gate beam (which is directly proportional to the strength of the THz beam) is measured using a quarter waveplate, polarizing prism and balance photodiodes. The time delay between the pump and the THz pulses at the sample position is controlled using optical delay stages. A final split-off of the laser is used to pump an optical parametric amplifier (Light Conversion: TOPAS-C) from which a 500 nm output is used as pump excitation.

UV-Vis Absorption Spectroscopy. A Perkin Elmer Lambda 950S was used to measure the transmittance and reflectance of films grown on the glass substrate. Deuterium and tungsten lamps are used as sources. It uses an integrating sphere to collect signals via the PMT and InGaAs detectors. The absorptance and hence the absorption was calculated based on the measured transmittance and reflectance data.

3. RESULTS AND DISCUSSION

3.1. CHEMICAL SYNTHESIS AND STRUCTURAL CHARACTERIZATION OF Ag_3SX POWDERS

Based on our previous work on the mechanochemical synthesis of different metal-halide materials,[38] we ball-milled stoichiometric amounts of Ag_2S and AgX (X = Br, I) for 1 h under inert atmosphere. However, this did not lead to the synthesis of Ag_3SI or Ag_3SBr, as shown in Figure 2a,c. Nevertheless, upon annealing at a moderate temperature of 160 °C for 30 min in nitrogen, Ag_3SI is formed from the ball-milled mixture of Ag_2S and AgI without any noticeable traces of unreacted precursors or by-products, as evidenced by the XRD analysis presented in Figure 2b. In the case of the bromide analogue, small traces of unreacted AgBr are still present after annealing at 160 °C (Figure S1), which vanish completely when the mixture is heated to 220 °C (Figure 2d). The composition and morphology of these powders were characterized by SEM and EDX, where no significant changes or deviations from the expected 3:1:1 stoichiometry were observed (Figure S2-S3 and Table S1).

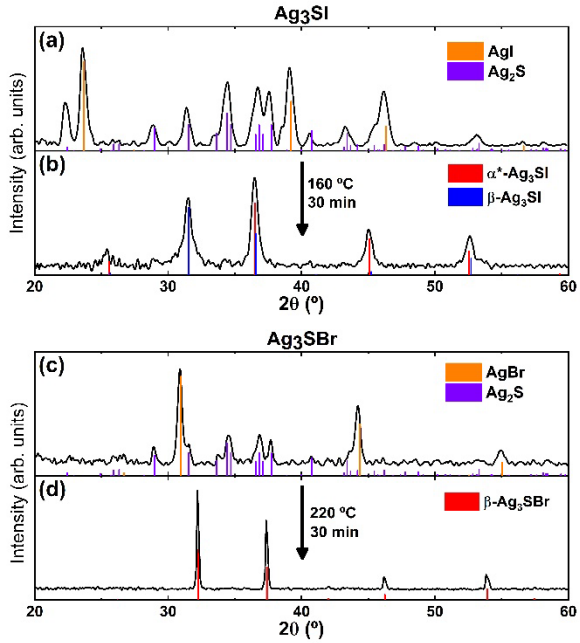

Figure 2. XRD of stoichiometric AgI+Ag_2S (a) and AgBr+Ag_2S (c) mixtures ball-milled for 1 h. XRD of resulting antiperovskite after thermal annealing in nitrogen at 160 °C (b) or 220 °C (d) for 30 min of (a) and (c), respectively. Reference patterns for AgI, AgBr, Ag_2S, α*-Ag3SI, β-Ag3SI, and β-Ag_3SBr correspond to Inorganic Crystal Structure Database (ICSD) entries #56552, #56546, #182916, #93429, #202123, and #25531, respectively. We must note a weak signal around 2θ=28° in Figure 2b whose origin is unclear.

Note that such thermal annealing at low temperature of pristine (non-ball-milled) powder mixtures does not yield the desired antiperovskite phase (see Figures S4 and S5), suggesting that both steps (ball-milling + thermal annealing) are necessary to obtain Ag_3SX. To be more precise on the obtained antiperovskite phases, we performed Rietveld refinement (whose details can be found as Supporting Information in Figure S6 and Table S2) of the XRD data which reveals a final composition of 75% α*-Ag_3SI and 25% β-Ag_3SI in the case of the iodide compound. In the case of X = Br, according to XRD (Figure S1), β-Ag_3SBr (cubic antiperovskite; space group *Pm-3m*) is formed at 220 °C and is stable at room temperature.[33] This analysis demonstrates that high-purity, non-templated Ag_3SX (X = I or Br) antiperovskites can be synthesized by a much faster and lower-temperature route compared to reported protocols in literature (see Table 1).

3.2. VISIBLE AND INFRARED LIGHT ABSORPTION CHARACTERIZATION

Determination of the absorption spectrum of powder samples by conventional transmission and reflection measurements is hampered by light scattering. We therefore used photothermal deflection spectroscopy (PDS; Figure 3) to characterize the optical response of Ag_3SX samples in the visible and near-infrared region. PDS measures the (relative) amount of heat produced upon photon absorption.[39] If the samples are not very emissive, as is the case here, only a tiny portion of the absorbed energy is re-emitted. Thus, for weakly emissive samples, almost all absorbed energy is converted to heat, resulting in a PDS spectrum proportional to the optical absorption spectrum. Note that, as opposed to transmission and reflection measurements, the PDS measurement is not affected by light scattering and if no absorption takes place, the PDS signal is zero. It is therefore ideally suited to characterize absorption onsets of highly scattering samples, such as powder samples.

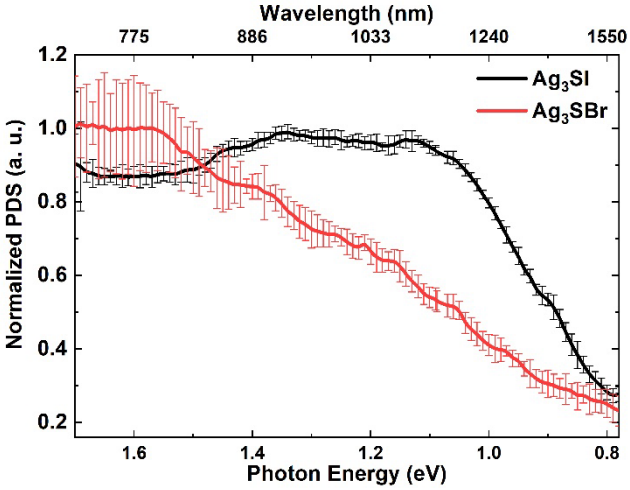

Figure 3. Photothermal deflection spectroscopy (PDS) characterization of Ag_3SI (black) and Ag_3SBr (red) powders. The PDS signal is proportional to the absorption spectrum. Error bars represent 95% confidence intervals.

The most striking feature in view of Figure 3 is the lack of a clear onset in the PDS signal that would allow for a clear determination of the bandgap energy value. This is especially so in the case of Ag_3SBr where a shallow slope is present from 0.8 eV to 1.55 eV. This spectrum is very similar to previous characterization of the same compound by the closely-related technique of photoacoustic spectroscopy and could be related to sub-bandgap absorption by impurities.[37] However, we note as well that similar shallow absorption onsets have also been reported for several multinary semiconductors (*e.g.*, kesterites, ABZ_2 semiconductors), which are attributed to lattice disorder.[40–42] Here, the disorder in the occupation of lattice sites has been shown to yield Gaussian disorder in the density of states, resulting in broad absorption tails. In any case, moving from X = Br to X = I seems to yield a red-shift in absorption similar to that

observed in tin and lead halide perovskites, with Ag_3SI showing strong absorption throughout the visible range as well as near infrared, which makes it promising for light-harvesting applications such as photovoltaics.

3.3. PULSED LASER DEPOSITION OF Ag_3SI THIN FILMS

Given the demonstrated fast and low-temperature synthesis of these silver chalcohalide antiperovskites and their promising properties for optoelectronics, we attempted the deposition of Ag_3SI thin films. Thermal single- and dual-source evaporation, which have proven to be suitable for lead-halide perovskites[43–45] were investigated with little success. No evidence of sulphur incorporation into the thin films was found, meaning that both the pre-synthesized Ag_3SI (in the single-source evaporation configuration) and Ag_2S (in the dual-source co-evaporation configuration) undergo decomposition and incongruent evaporation or sublimation with loss of sulphur at low temperatures (see Figures S7 and S8). In contrast, antiperovskite thin-films of around 140 nm thickness (Figure 4a) were successfully deposited by pulsed laser deposition (PLD) in a similar manner as recently reported for silver-bismuth-based halide double perovskites.[46] In brief, Ag_3SI powder is formed, first by mechanochemical synthesis, and then annealed as described in the Supporting Information. These stoichiometric powders are then pressed into a pellet and loaded into a PLD chamber. Ar gas is introduced to reach a working pressure of 1.5×10^{-2} mbar, after which an excimer laser (248 nm) ablates the target at a frequency of 10 Hz. The substrate is kept at room temperature for all depositions.

To begin with, the transfer of material from target to substrate was studied by energy dispersive X-ray spectroscopy (EDX). By tuning the PLD laser fluence from 2 J cm^{-2} to 0.3 J cm^{-2} we observe little effect on the incorporation of sulphur into the thin-films, which remain sulphur-poor. Instead, we find that the ratio of Ag:I can be tuned from 3.73 at 2 J cm^{-2} (an iodide deficiency) to 2.07 at 0.75 J cm^{-2} (an iodide excess) (Table S3). A fluence of 0.75 J cm^{-2} was chosen for this work, keeping an iodide excess in the film. This fluence was chosen in part to avoid the nucleation of metallic Ag crystals observed upon annealing of Ag-rich films (Figure S9). The sulphur deficiency was then compensated by adding an excess of elemental sulphur to the antiperovskite powder with a molar ratio of 3:1 before target pressing (see the Supporting Information for more details, Figure S10). Excess sulphur in the PLD target to compensate for its loss due to its high volatility was also reported previously for CuI:S.[47] Thin films deposited with these sulphur-rich targets were studied by EDX, and a sulphur excess was observed (Table 2). Samples were then annealed at 200 ^{0}C for 30 minutes in a nitrogen atmosphere, and then measured once again by EDX. After this annealing process, the ratios of Ag:I:S equalize to ~3:1:1 (Table 2). We note that in all post-annealed films a slight iodide-excess remains. This convergence towards the molar ratios expected for Ag_3SI is in agreement with XRD (Figure 4b), where the nucleation of Ag_3SI polymorphs is observed; the β-Ag_3SI phase being the most noticeable by its distinct peak at 31.65°. EDX spectra of the pristine and annealed thin-films is provided in Figures S11 and S12.

Table 2. EDX measurements of as-deposited and annealed films. All films were deposited at room temperature, 10 Hz repetition rate, 0.75 J cm^{-2} fluence, and a working pressure of 1.5 x 10^{-2} mbar. The samples were then annealed under N_2 at 200 ^{0}C for 30 minutes and show a convergence of the molar ratios of the Ag:S:I to ~3:1:1, with a slight iodide excess.

	Ag	S	I
Pristine	2.69	1.53	0.78
Annealed	2.93	0.97	1.10

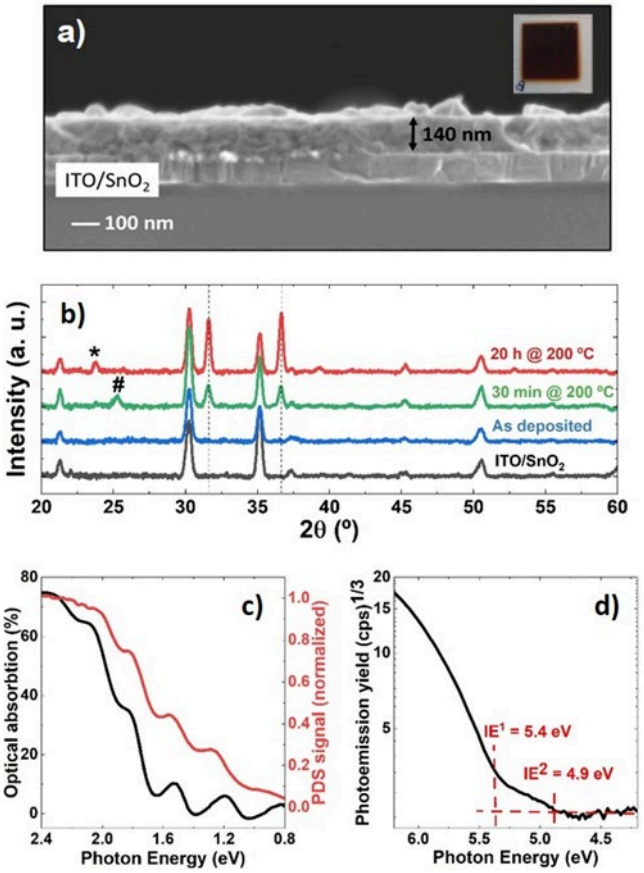

Figure 4. a) Cross-sectional SEM image of a Ag_3SI film deposited using a 3:1 S:Ag_3SI target and annealed for 20 hours at 200 ^{0}C; top view photograph as inset, substrate is 3x3cm. b) XRD of thin-films deposited using a sulphur-rich target of 3:1 S:Ag_3SI. These films were grown on an ITO/SnO_2 substrate whose diffraction pattern is shown in black. Peaks from AgI and α-Ag_3SI phases are denoted by * and #, respectively. c) Optical and PDS spectra. d) APS characterization showing ionization energy.

Upon further annealing for 20h, antiperovskite diffraction peaks become more intense, translating into an increased crystallization of amorphous material. A slight narrowing of diffraction peaks is also observed (see Figure S13) suggesting some crystallite growth and/or coalescence. The cross-sectional scanning electron microscopy

(SEM) of a film deposited using a 3:1 S:Ag_3SI target and subsequently annealed at 200 ^{0}C for 20 hr is shown in Figure 4a with a total thickness of 140 nm.

Optical properties of the annealed antiperovskite thin film are studied by PDS and UV-visible absorption (Figure 4c). In both cases a shallow slope is observed with multiple oscillations. These may be partly ascribed to interferences but also to structural disorder of the Ag^+ cations (see further discussion on theoretical calculations in the next section). Eventually photoelectron spectroscopy in air is carried out to determine the ionization energy (valence band maximum with respect to vacuum level). A linear extrapolation of the photoemission yield in linear scale gives an ionization energy around 5.4 eV (Figure S14). However, a closer look at the signal on a semi-logarithmic scale (Figure 4d) reveals a shallow density of states extending up to 4.9 eV. The origin of these features in the valence band maximum remains unclear but could also be related to structural disorder with the coexistence of α* and β phases as suggested by Figure 4b. Kelvin probe measurements (Figure S15) indicate a work function of 4.4 eV. Therefore, the Fermi level is calculated to be 0.5 to 1.0 eV above the valence band maximum.

In order to gain insights into the dynamics of photoexcited charge carriers in Ag_3SI thin films, we carried out transient OPTP photoconductivity spectroscopy measurements. Figure 5 shows a normalized OPTP transient measured for Ag_3SI following excitation with 2.48 eV pulses. As discussed by Wehrenfennig *et al.*,[48] the photoconductivity value immediately following the onset can be used to extract the effective electron-hole sum mobility in the material. This method has previously been used to extract charge-carrier mobilities for several emerging thin-film semiconductors (*e.g.*, lead halide perovskites, lead-free perovskites, and other perovskite-inspired materials).[49,50] Assuming free charge-carrier transport, we are able to extract an effective electron-hole sum mobility value of 49±1 $cm^2V^{-1}s^{-1}$. We note that the obtained mobility rivals that of lead halide perovskites and other emerging semiconductors.[51,52] To further analyze the lifetimes of charge carriers following excitation, the measured OPTP transient was fitted with a stretched exponential model revealing a short charge-carrier lifetime of τ~24 ps. Interestingly, the stretched exponential nature of the measured decay[53] indicates the strongly dispersive nature of charge-carrier recombination processes in these thin films which is compatible with a high level of disorder and the presence of defect-mediated recombination processes, in agreement with the observation of long and shallow absorption tails reported above.

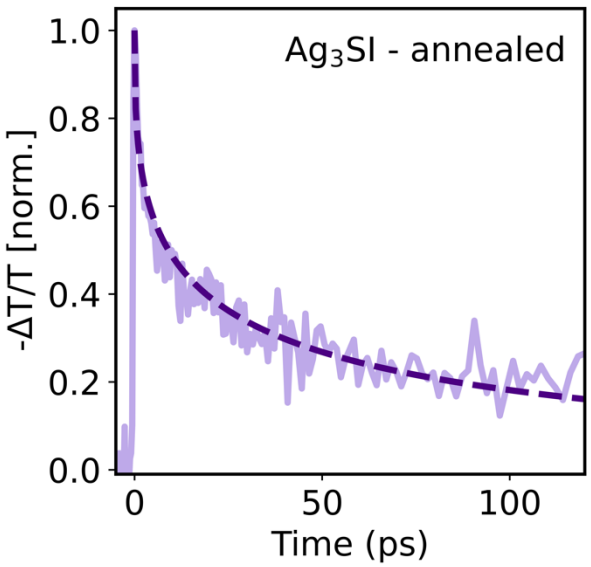

Figure 5. Normalized THz photoconductivity transient (-ΔT/T) of a Ag_3SI film annealed at 200 °C recorded following excitation with 2.48 eV photons at a pulse fluence of 0.9 μJ cm^{-2}. The dashed line corresponds to a stretched exponential fit to the experimental data.

Having extracted the charge carrier mobility and lifetime, we estimate a charge-carrier diffusion length of ~55 nm using the equation $L_D = (\mu\tau k_B T/e)^{1/2}$.[54] It is worth noting that the dispersive nature of charge-carrier recombination processes in Ag_3SI this film suggests that a range of charge-carrier recombination times are present, meaning that the obtained value represents an average diffusion length value.

3.4. THEORETICAL CALCULATIONS

To shed more light into the electronic properties of these silver chalcohalide antiperovskites, especially concerning the bandgap of Ag_3SBr on which very scarce and conflicting data is available (from 0.3 to 1.9 eV),[35–37] we undertook theoretical calculations at the DFT level using periodic boundary conditions (see the SI for computational details). Several phases have been previously characterized for Ag_3SI and Ag_3SBr.[33] In Ag_3SBr, the β phase is the one observed experimentally at room temperature, and consists of 3 Ag^+ ions distributed statistically into the 12(h) sites in a simple cubic structure with space group *Pm-3m*. Preliminary geometry optimizations indicate that the *Pm-3m* structure where the Ag ions are placed (averaged) at the face centers is unstable (transition state), and upon small atomic displacements it evolves to a γ-like distorted structure (see Figure S16a). On the other hand, the high-temperature α phase of Ag_3SI presents random distribution of S^{2-}/I^- anions, whose long-range ordering lowers the symmetry to *Pm-3m* (β phase).[55] As in Ag_3SBr, upon crystal relaxation of the *Pm-3m* cell of Ag_3SI, Ag ions move off the face center towards a *Cmcm*-like structure (Figure S16b). Further ordering of the Ag^+ cations in one of the four equivalent Ag-positions of the β phase leads to γ-Ag_3SI (space group *R3*).[55]

Minimum-energy crystal structures of Ag_3SBr and Ag_3SI were obtained at the PBEsol/light tier-1 level of theory using primitive, conventional, and extended unit cells (see Figure S17). Lattice parameters for all the crystal structures

are summarized in Table S3. High-level theoretical calculations using the hybrid HSE06 functional and including spin-orbit coupling (SOC) predict an indirect(T→Γ)/direct(Γ) bandgap (E_g) of 1.49/1.66 eV (Figure S14-S15), in contrast to a value of 0.88 eV reported at the less-accurate LDA level of theory,[56] but in good accord with photoacoustic experiments (1.5 and 1.85 eV for a broad absorption shoulder and peak, respectively).[37] The effect of the functional used in the calculations and the SOC correction on the bandgap energy is detailed in Table S4. The bandgap of Ag_3SBr is characterized by a valence-band maximum (VBM) with an even contribution of constituting Ag^+ (4d-orbitals), S^{2-} (3p-orbitals), and Br^- (4p-orbitals) ions, whereas the conduction-band minimum (CBM) mainly involves the 5s-orbital of Ag^+ (Figure 6a and S18-S19). These results therefore evidence the crucial role of Ag in the VBM/CBM nature and suggest that the Ag ordering within the crystal may influence the bandgap energy.

Enlarging the unit cell from primitive to conventional and extended orthorhombic (ORC) cells increases the Ag^+ degrees of freedom for further relaxation and symmetry alleviation, and leads to a small decrease of the bandgap to 1.42/1.58 eV (indirect/direct) and 1.44 eV, respectively (Table S5). These values are in line with the reported experimental photoacoustic data and with our powder PDS signal saturation (*ca.* 1.55 eV). The electronic band structure found for the conventional ORC unit cell of Ag_3SBr is displayed in Figure 6b, showing a large number of quasi-degenerated states below the bandgap indicative of high disorder of Ag^+ ions within the cell.

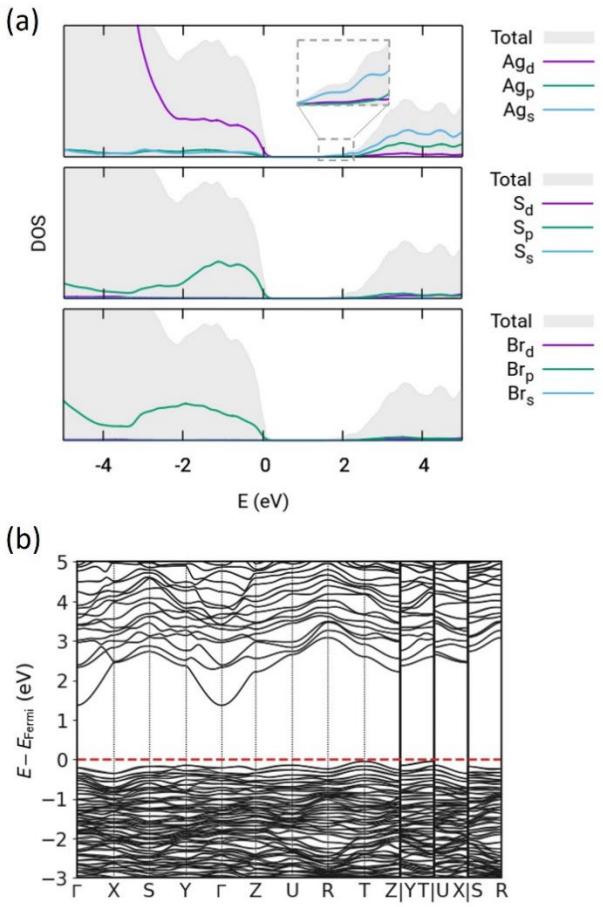

Figure 6. Mulliken orbital-projected density of states (a) and band structure (b) calculated at the HSE06+SOC level for the conventional ORC cell of Ag_3SBr.

Moving to Ag_3SI, an HSE06+SOC indirect(S→Γ)/direct(Γ) bandgap of 1.28/1.56 eV is predicted for the β-ORCC primitive cell (Figure S20-S21). For the sake of comparison, the γ phase of Ag_3SI (space group *R3*) is predicted with a bandgap of 1.34/1.71 eV for primitive rhombohedral and 1.32/1.69 eV for conventional hexagonal cells (Table S3 and Figure S17-S18). As in Ag_3SBr, Ag orbitals are highly involved in the VBM (4d-orbitals) and CBM (5s-orbital) of β- Ag_3SI (Figure S22). Moving from primitive ORCC to conventional and extended ORC cells leads to a noticeable bandgap reduction up to 0.82(Z→Γ)/1.06(Γ) and 1.00 eV, respectively (Figure S23-S27 and Table S5). This bandgap reduction is prompted by zig-zag Ag^+ ions displacements from *Cmcm* out of *ab*-plane along the *c*-axis (Figure 7). Simulation of the absorption spectrum by means of the linear macroscopic dielectric function approximation nicely matches the PDS shape recorded experimentally for the Ag_3SI film, with several shoulders in the low-energy range (compare Figure 4c and Figure S28).

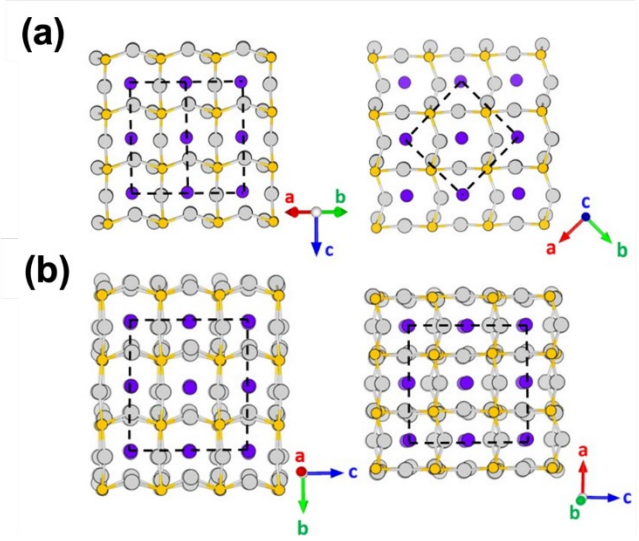

Figure 7. Minimum-energy crystal structures calculated at the PBEsol level for the primitive ORCC (a) and conventional ORC (b) unit cells of β-Ag_3SI. Color coding: gray for Ag, yellow for S, and purple for I.

On the other hand, the α* phase of Ag_3SI was modelled by randomly exchanging 15% and 100% of the S^{2-}/I^- anions in the conventional ORC unit cell. Minimum–energy crystal structures indicate large deformations localized over the defectively positioned anions in the 15% model, whereas a fully disordered structure is predicted for 100% exchange (see Figure S29). Theoretical calculations at the HSE06+SOC level predict for α*-Ag_3SI a significant increase in the indirect/direct bandgap from 0.82/1.06 eV (β phase) to 1.30/1.31 eV (15% random distribution) and 1.29/1.39 eV (100% random distribution), in good accordance with the experimental evidences.[57]

Finally, the thermal effect on the bandgap was disentangled by performing ab-initio Car-Parrinello molecular dynamics on Ag_3SBr and Ag_3SI for 1 ps simulation time at 300 K (see the SI for details). Theoretical calculations predict a negligible thermal effect on the bandgap of Ag_3SBr compared to the static calculations, with an average value of 1.42±0.07(indirect)/1.47±0.08(direct) eV. In contrast, the bandgap of Ag_3SI experiences a noticeable increase of ca. 0.3 eV during the dynamics, with an average E_g of 1.14±0.14(indirect)/1.38±0.14(direct) eV. In spite of this, root-mean-standard deviation (RMSD) in atomic displacements indicate that silver atoms have moved more on average in Ag_3SBr (RMSD of Ag = 1.11 Å) than in Ag_3SI (RMSD of Ag = 0.85 Å; see Table S6), suggesting that the electronic structure of the iodine-based material is more sensitive to local distortions.

4. CONCLUSIONS

In conclusion, we have shown the fast (< 2 h) and solvent-free synthesis of Ag_3SI and Ag_3SBr antiperovskites through mechanochemical synthesis and thermal annealing at moderate temperatures (160 °C and 220 °C, respectively). Thin films of Ag_3SI were successfully deposited by pulsed-laser deposition from S-enriched Ag_3SI targets. Our analysis of THz photoconductivity demonstrates that Ag_3SI films present a high charge-carrier mobility of 49 $cm^2V^{-1}s^{-1}$. However, the relatively fast recombination lifetimes show that development of targeted trap passivation techniques is urgently required in order to extend charge-carrier diffusion lengths towards the hundreds of nanometers. Altogether, we believe that these findings highlight the great potential of silver chalcohalide antiperovskites for optoelectronic applications and elucidate the next challenges which need to be addressed in order to improve the fabrication and performances of this promising class of emerging materials.

ASSOCIATED CONTENT

Supporting Information.
This material is available free of charge via the Internet at http://pubs.acs.org.
XRD of in-situ annealing of Ag_3SBr, XRD of hand-mixed precursors, Rietveld refinement of Ag_3SI, computed crystal structures and lattice parameters, calculated density of states, calculated band structures and bandgap energies, XRD of thin films by single- and dual-source sublimation, EDX and XRD of films by PLD, XRD of PLD targets, details of Optical-Pump-Terahertz-Probe Measurements.

AUTHOR INFORMATION

Corresponding Authors

Francisco Palazon. Instituto de Ciencia Molecular, ICMol, Universidad de Valencia, 46980 Paterna, Spain; Departamento de Ingeniería Química y Ambiental, Universidad Politécnica de Cartagena, 30202 Cartagena, Spain; https://orcid.org/0000-0002-1503-5965
Email: francisco.palazon@upct.es, francisco.palazon@uv.es

Henk J. Bolink. Instituto de Ciencia Molecular, ICMol, Universidad de Valencia, 46980 Paterna, Spain; https://orcid.org/0000-0001-9784-6253
Email: henk.bolink@uv.es

Authors

Paz Sebastia-Luna. Instituto de Ciencia Molecular, ICMol, Universidad de Valencia, 46980 Paterna, Spain; https://orcid.org/0000-0001-6992-199X

Nathan Rodkey. Instituto de Ciencia Molecular, ICMol, Universidad de Valencia, 46980 Paterna, Spain; MESA+ Institute for Nanotechnology, University of Twente, Enschede 7500 AE, The Netherlands; https://orcid.org/0000-0003-4246-3911

Adeem Saeed Mirza. MESA+ Institute for Nanotechnology, University of Twente, Enschede 7500 AE, The Netherlands https://orcid.org/0000-0003-1217-6858

Sigurd Mertens. Institute for Materials Research (IMO-IMOMEC), Hasselt University, Diepenbeek BE – 3590, Belgium.

Snigdha Lal. Department of Physics, University of Oxford, Clarendon Laboratory, Parks Road, Oxford OX1 3PU, UK. https://orcid.org/0000-0002-3086-1990

Axel M. Gaona-Carranza. Instituto de Ciencia Molecular, Universidad de Valencia, 46980 Paterna, Spain; https://orcid.org/0000-0001-5911-1512

Joaquín Calbo. Instituto de Ciencia Molecular, Universidad de Valencia, 46980 Paterna, Spain;
https://orcid.org/0000-0003-4729-0757

Marcello Righetto. Department of Physics, University of Oxford, Clarendon Laboratory, Parks Road, Oxford OX1 3PU, UK.
https://orcid.org/0000-0001-5507-1445

Michele Sessolo. Instituto de Ciencia Molecular, Universidad de Valencia, 46980 Paterna, Spain.

Laura M. Herz. Department of Physics, University of Oxford, Clarendon Laboratory, Parks Road, Oxford OX1 3PU, UK, Institute for Advanced Study, Technical University of Munich, Lichtenbergstrasse 2a, D-85748 Garching, Germany.
https://orcid.org/0000-0001-9621-334X

Koen Vandewal. Institute for Materials Research (IMO-IMOMEC), Hasselt University, Diepenbeek BE – 3590, Belgium;
https://orcid.org/0000-0001-5471-383X

Enrique Ortí. Instituto de Ciencia Molecular, Universidad de Valencia, 46980 Paterna, Spain;
https://orcid.org/0000-0001-9544-8286

Mónica Morales-Masis. MESA+ Institute for Nanotechnology, University of Twente, Enschede 7500 AE, The Netherlands;
https://orcid.org/0000-0003-0390-6839

Author Contributions

The manuscript was written through contributions of all authors.

Notes

The authors declare no competing financial interest.

ACKNOWLEDGMENT

The research leading to these results has received funding from the European Research Council (ERC) under the European Union's Horizon 2020 research and innovation programme (grant agreement No. 834431). Authors acknowledge support from the Comunitat Valenciana (IDIFEDER/2018/061, GV/2021/027, PROMETEU/2020/077 and CISEJI/2022/43), as well as by the Ministry of Science and Innovation (MCIN) and the Spanish State Research Agency (AEI) (projects PID2020-119748GA-I00, PID2021-128569NB-I00, and CEX2019-000919-M, funded by MCIN/AEI/10.13039/501100011033 and by "ERDF A way of making Europe", project TED2021-131255B-C44 funded by MCIN/AEI/10.13039/501100011033 and by European Union NextGenerationEU/PRTR, grants RYC-2016-21316 and RYC2020-028803-I funded by MCIN/AEI/10.13039/501100011033 and "ESF Investing in your future"). Dutch Research Council (NWO, FOM Focus Group "Next Generation Organic Photovoltaics"). P. S. thanks the Spanish Ministry of Universities for her pre-doctoral grant (FPU18/01732 and EST19/00295). ASM and MMM acknowledge the financial support of the NWO StartUp 2019 project BRIDGE (project number: STU.019.026). M.R and L.M.H acknowledge financial support from the Engineering and Physical Sciences Research Council UK. S.L. acknowledges funding from the Oxford India Centre for Sustainable Development. F.P. thanks Dr. Quinten A. Akkerman for first telling him about these materials in 2019 in a conversation that sparked the research leading to the results presented herein.

REFERENCES

(1) Akkerman, Q. A.; Manna, L. What Defines a Halide Perovskite? *ACS Energy Letters* **2020**, 604–610. https://doi.org/10.1021/acsenergylett.0c00039.

(2) Wells, H. L. Über Die Cäsium- Und Kalium- Bleihalogenide. *Zeitschrift für anorganische und allgemeine Chemie* **1893**, *3* (1), 195–210. https://doi.org/10.1002/zaac.18930030124.

(3) Reuter, B.; Hardel, K. Silbersulfidbromid Und Silbersulfidjodid. *Angewandte Chemie* **1960**, *72* (4), 138–139. https://doi.org/10.1002/ange.19600720407.

(4) Chiodelli, G.; Magistris, A.; Schiraldi, A. Ag3SBr and Ag3SI: Ionic Conductivity of Their Modifications in the Range 93—573 K. *Zeitschrift für Physikalische Chemie Neue Folge* **1979**, *118*, 177–186.

(5) Spinolo, G.; Massarotti, V. Ag3SBr and Ag3SI a Diffractometric Study of the Low Temperature Modifications. *Zeitschrift fur Physikalische Chemie* **1980**, *121* (1), 7–15. https://doi.org/10.1524/zpch.1980.121.1.007.

(6) Kawamura, J.; Siitmoji, M.; Hoshino, H. The Ionic Conductivity and Thermoelectric Power of the Superionic Conductor Ag3SBr. *Journal of the Physical Society of Japan* **1981**, *50* (1), 194–200. https://doi.org/10.1143/JPSJ.50.194.

(7) Kennedy, J. H.; Chen, F. Solid Electrolyte Coulometry. Silver Sulfide Bromide Electrolyte. *Electrochem Soc-J* **1969**, *116* (2), 207–211.

(8) Magistris, A.; Chiodelli, G.; Schiraldi, A. Low Temperature Phase Transitions of Ag3SBr and Ag3SI. *Zeitschrift fur Physikalische Chemie* **1978**, *112* (2), 251–253. https://doi.org/10.1524/zpch.1978.112.2.251.

(9) Reuter, B.; Hardel, K. Silbersulfidbromid Ag3SBr Und Silbersulfidjodid Ag3SJ. II. Die Kristallstrukturen von Ag3SBr, B- Und A-Ag3SJ. *ZAAC - Zeitschrift für anorganische und allgemeine Chemie* **1965**, *340* (3–4), 168–180. https://doi.org/10.1002/zaac.19653400308.

(10) Reuter, B.; Hardel, K. Silbersulfidbromid Und Silbersulfidjodid. *Angewandte Chemie* **1960**, *72* (4), 138–139. https://doi.org/10.1002/ange.19600720407.

(11) Reuter, B.; Hardel, K. Über Die Hochtemperaturmodifikation von Silbersulfidjodid. *Kurze Originalmitteilungen* **1961**, *48*, 161.

(12) Kurita, M.; Nakagawa, K.; Wakamura, K. Fundamental Absorption Edge of α-AgI-Type Superionic Conductor Ag3SBr. *Japanese Journal of Applied Physics, Part 1: Regular Papers and Short Notes and Review Papers* **2000**, *39* (4 A), 1786–1787.

(13) Xianglian, H. H.; Basar, K.; Siagian, S.; Sakuma, T.; Takahashi, H.; Tubuqinbaer; Kawaji, H.; Atake, T. Low-Temperature Phase in Superionic Conductor Ag 3SBr XI 1-x. *Journal of the Physical Society of Japan* **2007**, *76* (11), 3–6. https://doi.org/10.1143/JPSJ.76.114603.

(14) Kurita, M.; Nakagawa, K.; Akao, F. Photoacoustic Spectrum in Superionic Conductors Ag3SI and AgI. *Japanese Journal of Applied Physics* **1988**, *27* (10 A), L1920–L1922. https://doi.org/10.1143/JJAP.27.L1920.

(15) Takahashi, T.; Yamamoto, O. The Ag/Ag3SI/I2 Solid-Electrolyte Cell. *Electrochimica Acta* **1966**, *11* (7), 779–789. https://doi.org/10.1016/0013-4686(66)87055-X.

(16) Hoshino, S.; Sakuma, T.; Fujii, Y. A Structural Phase Transition in Superionic Conductor Ag3SI. *Journal of the Physical Society of Japan* **1979**, *47* (4), 1252–1259. https://doi.org/10.1143/JPSJ.47.1252.

(17) Hoshino, S.; Fujishita, H.; Takashige, M.; Sakuma, T. Phase Transition of Ag3SX (X=I, Br). *Solid State Ionics* **1981**, *3–4* (C), 35–39. https://doi.org/10.1016/0167-2738(81)90050-3.

(18) Yin, L.; Murphy, M.; Kim, K.; Hu, L.; Cabana, J.; Siegel, D. J.; Lapidus, S. H. Synthesis of Antiperovskite Solid Electrolytes: Comparing Li3SI, Na3SI, and Ag3SI. *Inorganic Chemistry* **2020**, *59* (16), 11244–11247. https://doi.org/10.1021/acs.inorgchem.0c01705.

(19) Hull, S.; Keen, D. A.; Gardner, N. J. G.; Hayes, W. The Crystal Structures of Superionic Ag3SI. *Journal of Physics Condensed Matter* **2001**, *13* (10), 2295–2316. https://doi.org/10.1088/0953-8984/13/10/321.

(20) Tver'yanovich, Y. S.; Bal'makov, M. D.; Tomaev, V. V.; Borisov, E. N.; Volobueva, O. Ion-Conducting Multilayer Films Based on Alternating Nanolayers Ag 3SI, AgI and Ag2S, AgI. *Glass Physics and Chemistry* **2008**, *34* (2), 150–154. https://doi.org/10.1134/S1087659608020065.

(21) Kojima, A.; Hoshino, S.; Noda, Y.; Fujii, K.; Kanashiro, T. Modified Bridgman Growth of Centimeter-Large Single Crystals of the Solid Electrolyte Ag3SI. *Journal of Crystal Growth* **1989**, *94* (2), 293–298. https://doi.org/10.1016/0022-0248(89)90002-X.

(22) Wakamura, K.; Miura, F.; Kojima, A.; Kanashiro, T. Observation of Anomalously Increasing Phonon Damping Constant in the Phase of the Fast-Ionic Conductor Ag3SI. *Physical Review B* **1990**, *41* (5), 2758–2762. https://doi.org/10.1103/PhysRevB.41.2758.

(23) Beeken, R. B.; Wright, T. J.; Sakuma, T. Effect of Chloride Substitution in the Fast Ion Conductor Ag3SBr. *Journal of Applied Physics* **1999**, *85* (11), 7635–7638. https://doi.org/10.1063/1.370565.

(24) Beeken, R. B.; Beeken, E. M. Ionic Conductivity in Cu-Substituted Ag3SBr. *Solid State Ionics* **2000**, *136–137*, 463–467. https://doi.org/10.1016/S0167-2738(00)00564-6.

(25) Beeken, R. B.; Jetzer, W. L.; Smith, D. R. Ionic Conduction in Cd-Substituted Ag3SBr. *Solid State Ionics* **1994**, *70/71*, 176–179.

(26) Beeken, R. B.; Haase, A. T.; Hoerman, B. H.; Klawikowski, S. J. The Effect of Non-Stoichiometry in Ag3SBr. *Solid State Ionics* **1998**, *113–115*, 509–513. https://doi.org/10.1016/s0167-2738(98)00384-1.

(27) Yan, S.; Xiao, H.; Liu, X. Rapid Fabrication and Thermal Performance of Ag 3 Si Super-Ionic Conductor. *Chalcogenide Letters* **2016**, *13* (10), 483–487.

(28) Huber, H.; Mali, M.; Roos, J.; Brinkmann, D. Test of Diffusion Models for the Superionic Conductor - Ag3SBr by Silver NMR at 1 Bar and 7 Kbar. *Physical Review B* **1988**, *37* (4), 1441–1447. https://doi.org/10.1103/PhysRevB.37.1441.

(29) Huber, H.; Mali, M.; Roos, J.; Brinkmann, D. Diffusion and Pressure Effects in the Superionic Conductor Ag3SBr Studied by NMR. *Solid State Ionics* **1986**, *18–19* (PART 2), 1188–1192. https://doi.org/10.1016/0167-2738(86)90331-0.

(30) Huber, H.; Mali, M.; Roos, J.; Brinkmann, D. NMR Relaxation at Pressures up to 7 Kbar in the Superionic Conductor Ag3SBr. *Physica B+C* **1986**, *139–140* (C), 289–291. https://doi.org/10.1016/0378-4363(86)90580-2.

(31) Gras, B.; Funke, K. Non-Periodic Local Motion of Silver Ions in ß-Ag3SI from Far-Infrared Conductivity Measurements. *Solid State Ionics* **1981**, 341–346.

(32) Yin, L.; Murphy, M.; Kim, K.; Hu, L.; Cabana, J.; Siegel, D. J.; Lapidus, S. H. Synthesis of Antiperovskite Solid Electrolytes: Comparing Li3SI, Na3SI, and Ag3SI. *Inorganic Chemistry* **2020**, *59* (16), 11244–11247. https://doi.org/10.1021/acs.inorgchem.0c01705.

(33) Sakuma, T.; Hoshino, S. The Phase Transition and the Structures of Superionic Conductor Ag3SBr. *Journal of the Physical Society of Japan* **1980**, *49* (2), 678–683. https://doi.org/10.1143/JPSJ.49.678.

(34) Shimosaka, W.; Kashida, S.; Kobayashi, M. Electronic Structure of Ag3SI. *Solid State Ionics* **2005**, *176* (3–4), 349–355. https://doi.org/10.1016/j.ssi.2004.08.001.

(35) Materials Project. *Ag3SBr - mp-1105645*. https://doi.org/10.1063/1.4812323.

(36) Materials Project. *Ag3SI - mp-558189*. https://doi.org/10.1038/SDATA.2018.151.

(37) Kurita, M.; Nakagawa, K.; Wakamura, K. Fundamental Absorption Edge of α-AgI-Type Superionic Conductor Ag3SBr. *Japanese Journal of Applied Physics, Part 1: Regular Papers and Short Notes and Review Papers* **2000**, *39* (4 A), 1786–1787. https://doi.org/10.1143/jjap.39.1786.

(38) Palazon, F.; Ajjouri, Y. El; Bolink, H. J. Making by Grinding : Mechanochemistry Boosts the Development of Halide Perovskites and Other Multinary Metal Halides. *Advanced Energy Materials* **2019**, *1902499*, 1–13. https://doi.org/10.1002/aenm.201902499.

(39) Jackson, W. B.; Amer, N. M.; Boccara, A. C.; Fournier, D. Photothermal Deflection Spectroscopy and Detection. *Applied Optics* **1981**, *20* (8), 1333–1344. https://doi.org/10.1364/AO.20.001333.

(40) Gokmen, T.; Gunawan, O.; Todorov, T. K.; Mitzi, D. B. Band Tailing and Efficiency Limitation in Kesterite Solar Cells. *Applied Physics Letters* **2013**, *103506 (1-5)*.

(41) Rey, G.; Larramona, G.; Bourdais, S.; Choné, C.; Delatouche, B.; Jacob, A.; Dennler, G.; Siebentritt, S. On the Origin of Band-Tails in Kesterite. *Solar Energy Materials and Solar Cells* **2017**, No. November, 1–10. https://doi.org/10.1016/j.solmat.2017.11.005.

(42) Wang, Y.; Kavanagh, S. R.; Burgués-Ceballos, I.; Walsh, A.; Scanlon, D. O.; Konstantatos, G. Cation Disorder Engineering Yields AgBiS2 Nanocrystals with Enhanced Optical Absorption for Efficient Ultrathin Solar Cells. *Nature Photonics* **2022**, *16*, 235–241.

(43) Momblona, C.; Gil-Escrig, L.; Bandiello, E.; Hutter, E. M.; Sessolo, M.; Lederer, K.; Blochwitz-Nimoth, J.; Bolink, H. J. Efficient Vacuum Deposited P-i-n and n-i-p Perovskite Solar Cells Employing Doped Charge Transport Layers. *Energy Environ. Sci.* **2016**, *9* (11), 3456–3463. https://doi.org/10.1039/C6EE02100J.

(44) Choi, H.; Jeong, J.; Kim, H. B.; Kim, S.; Walker, B.; Kim, G. H.; Kim, J. Y. Cesium-Doped Methylammonium Lead Iodide Perovskite Light Absorber for Hybrid Solar Cells. *Nano Energy* **2014**, *7*, 80–85. https://doi.org/10.1016/J.NANOEN.2014.04.017.

(45) El Ajjouri, Y.; Palazon, F.; Sessolo, M.; Bolink, H. J. Single-Source Vacuum Deposition of Mechanosynthesized Inorganic Halide Perovskites. *Chemistry of Materials* **2018**, *30*, 7423–7427. https://doi.org/10.1021/acs.chemmater.8b03352.

(46) Rodkey, N.; Kaal, S.; Sebastia-Luna, P.; Birkhölzer, Y. A.; Ledinsky, M.; Palazon, F.; Bolink, H. J.; Morales-Masis, M. Pulsed Laser Deposition of Cs2AgBiBr6: From Mechanochemically Synthesized Powders to Dry, Single-Step Deposition. *Chemistry of Materials* **2021**, *33* (18), 7417–7422. https://doi.org/10.1021/acs.chemmater.1c02054.

(47) Mirza, A. S.; Pols, M.; Soltanpoor, W.; Tao, S.; Brocks, G.; Morales-Masis, M. Sulphur-Doped Copper(I) Iodide as Record Figure of Merit P-Type Transparent Conductor. Rochester, NY May 18, 2023. *Paper under review, Matter,* **2023** https://doi.org/10.2139/ssrn.4450373.

(48) Wehrenfennig, C.; Eperon, G. E.; Johnston, M. B.; Snaith, H. J.; Herz, L. M. High Charge Carrier Mobilities and Lifetimes in Organolead Trihalide Perovskites. *Advanced Materials* **2014**, 1584–1589. https://doi.org/10.1002/adma.201305172.

(49) Buizza, L. R. V; Sansom, H. C.; Wright, A. D.; Ulatowski, A. M.; Johnston, M. B.; Snaith, H. J.; Herz, L. M. Interplay of Structure , Charge-Carrier Localization and Dynamics in Copper-Silver-Bismuth-Halide Semiconductors. *Advanced Functional Materials* **2021,** 2108392 (1-15) https://doi.org/10.1002/adfm.202108392.

(50) Jia, Z.; Righetto, M.; Yang, Y.; Xia, C. Q.; Li, Y.; Li, R.; Li, Y.; Yu, B.; Liu, Y.; Huang, H.; Johnston, M. B.; Herz, L. M.; Lin, Q. Charge-Carrier Dynamics of Solution-Processed Antimony- and Bismuth-Based Chalcogenide Thin Films. *ACS Energy Lett.* **2023**, *8* (3), 1485–1492.

(51) Kober-Czerny, M.; Motti, S. G.; Holzhey, P.; Wenger, B.; Lim, J.; Herz, L. M.; Snaith, H. J. Excellent Long-Range Charge-Carrier Mobility in 2D Perovskites. *Advanced Functional Materials* **2022**, *32* (36), 2203064 (1-10). https://doi.org/10.1002/adfm.202203064.

(52) Herz, L. M. Charge-Carrier Mobilities in Metal Halide Perovskites: Fundamental Mechanisms and Limits. *ACS Energy Letters* **2017**, *2* (7), 1539–1548. https://doi.org/10.1021/acsenergylett.7b00276.

(53) Johnston, D. C. Stretched Exponential Relaxation Arising from a Continuous Sum of Exponential Decays. *Physical Review B - Condensed Matter and Materials Physics* **2006**, *74* (18), 1–7. https://doi.org/10.1103/PhysRevB.74.184430.

(54) Buizza, L. R. V.; Crothers, T. W.; Wang, Z.; Patel, J. B.; Milot, R. L.; Snaith, H. J.; Johnston, M. B.; Herz, L. M. Charge-Carrier Dynamics, Mobilities, and Diffusion Lengths of 2D–3D Hybrid Butylammonium–Cesium–Formamidinium Lead Halide Perovskites. *Advanced Functional Materials* **2019**, *29* (35), 1902656 (1-9). https://doi.org/10.1002/adfm.201902656.

(55) Hull, S.; Keen, D. A.; Gardner, N. J. G.; Hayes, W. The Crystal Structures of Superionic Ag3SI. *Journal of Physics Condensed Matter* **2001**, *13* (10), 2295–2316. https://doi.org/10.1088/0953-8984/13/10/321.

(56) Shimosaka, W.; Kashida, S.; Kobayashi, M. Electronic Structure of Ag3SI. *Solid State Ionics* **2005**, *176* (3–4), 349–355. https://doi.org/10.1016/j.ssi.2004.08.001.

(57) Kurita, M.; Nakagawa, K.; Akao, F. Photoacoustic Spectrum in Superionic Conductors Ag3SI and AgI. *Japanese Journal of Applied Physics* **1988**, *27* (10 A), L1920–L1922. https://doi.org/10.1143/JJAP.27.L1920.

Authors are required to submit a graphic entry for the Table of Contents (TOC) that, in conjunction with the manuscript title, should give the reader a representative idea of one of the following: A key structure, reaction, equation, concept, or theorem, etc., that is discussed in the manuscript. Consult the journal's Instructions for Authors for TOC graphic specifications.

Insert Table of Contents artwork here